

Article

Synergism of Artificial Intelligence and Techno-Economic for Sustainable Treatment of Methylene Blue Dye-Containing Wastewater by Photocatalysis

Khumbolake Faith Ngulube ¹ , Amal Abdelhaleem ¹ , Manabu Fujii ² and Mahmoud Nasr ^{1,3,*} 

¹ Environmental Engineering Department, Egypt-Japan University of Science and Technology (E-JUST), Alexandria 21934, Egypt; khumbolake.ngulube@ejust.edu.eg (K.F.N.); amal.elsonbaty@ejust.edu.eg (A.A.)

² Civil and Environmental Engineering Department, Tokyo Institute of Technology, Meguro-Ku, Tokyo 152-8552, Japan; fujii.m.ah@m.titech.ac.jp

³ Sanitary Engineering Department, Faculty of Engineering, Alexandria University, Alexandria 21544, Egypt

* Correspondence: mahmoud.nasr@ejust.edu.eg; Tel.: +20-1006-390-400

Abstract: Recently, removing dyes from wastewater by photocatalysis has been extensively studied by several researchers. However, there exists a research gap in optimizing the photocatalytic process parameters using artificial intelligence to maintain the associated techno-economic feasibility. Hence, this investigation attempts to optimize the photocatalytic degradation of methylene blue (MB) dye using an artificial neural network (ANN) model to minimize the capital and running costs, which is beneficial for industrial applications. A ZnO/MgO photocatalyst was synthesized, showing an energy band gap of 2.96 eV, crystallinity index of 71.92%, pore volume of 0.529 cm³/g, surface area of 30.536 m²/g, and multiple surface functional groups. An ANN model, with a 4-8-1 topology, *trainlm* training function, and feed-forward back-propagation algorithm, succeeded in predicting the MB removal efficiency ($R^2 = 0.946$ and mean squared error = 11.2). The ANN-based optimized condition depicted that over 99% of MB could be removed under $C_0 = 16.42$ mg/L, pH = 9.95, and catalyst dosage = 905 mg/L within 174 min. This optimum condition corresponded to a treatment cost of USD 8.52/m³ cheaper than the price estimated from the unoptimized photocatalytic system by $\approx 7\%$. The study outputs revealed positive correlations with the sustainable development goals accompanied by pollution reduction, human health protection, and aquatic species conservation.

Keywords: ANN optimization; dye degradation; nanocomposite characterization; photocatalytic performance; treatment cost



Citation: Ngulube, K.F.; Abdelhaleem, A.; Fujii, M.; Nasr, M. Synergism of Artificial Intelligence and Techno-Economic for Sustainable Treatment of Methylene Blue Dye-Containing Wastewater by Photocatalysis. *Sustainability* **2024**, *16*, 529. <https://doi.org/10.3390/su16020529>

Academic Editors: Ying Zhang and Fangke Yu

Received: 12 December 2023

Revised: 31 December 2023

Accepted: 2 January 2024

Published: 8 January 2024



Copyright: © 2024 by the authors. Licensee MDPI, Basel, Switzerland. This article is an open access article distributed under the terms and conditions of the Creative Commons Attribution (CC BY) license (<https://creativecommons.org/licenses/by/4.0/>).

1. Introduction

Discharging methylene blue (MB)-laden wastewater into the aquatic environment without proper treatment can impose several negative impacts on the health status of water bodies [1]. For instance, the MB dye can form a colored layer on the water surface [2], preventing light penetration into the marine environment that contains plant and aquatic species [3]. The sunlight absorption and scattering problems could also delay the photosynthetic processes of aquatic plants and reduce the dissolved oxygen availability for marine life [4]. Moreover, exposure of humans to high concentrations of MB can cause serious health problems and dangerous injuries, such as increased heart rate, shock, jaundice, tissue necrosis, vomiting, and cyanosis [5]. As a result of these negative impacts, MB-containing effluents must be efficiently treated before their release into the environmental dimensions.

MB has a complex and recalcitrant molecular structure, allowing it to persist in the environment for long periods and hindering its removal from wastewater by conventional treatment techniques [6]. For instance, the biological degradation of MB requires an extended retention time and certain enzymatic reactions to ensure the microbial breakdown scheme. Moreover, removing MB from wastewater by its adsorption into a certain material

creates secondary pollution via disposal of the exhausted adsorbent [7]. Alternatively, various researchers have employed advanced oxidation processes (AOPs) to eliminate MB from aqueous solutions via decomposition and mineralization [3,8,9].

Heterogeneous photocatalysis (semiconductor photocatalysis) is a widely used AOP, having a great potential to degrade multiple pollutants under low energy conditions such as visible light and sunlight irradiation [10,11]. In this process, the photocatalyst material absorbs photon energy equal or greater in magnitude to the energy band gap of the semiconductor material [12]. This absorbed energy excites an electron (e^-) from the valence to the conduction band of the photocatalyst material across the energy band gap [13]. This e^- excitation scheme leaves a hole (h^+) behind in the valence band, where the electron-hole pairs interact with H_2O to form $\bullet OH$ ($H_2O + h^+ \rightarrow \bullet OH + H^+$) and O_2 to create $\bullet O_2^-$ ($O_2 + e^- \rightarrow \bullet O_2^-$) [14]. These generated highly reactive oxygen species (ROS) participate in a series of REDOX reactions to degrade pollutants (e.g., dyes) into simpler compounds such as CO_2 and H_2O [15].

Zinc oxide (ZnO) and magnesium oxide (MgO) are two semiconductors that have been involved in the photocatalytic degradation of various pollutants. However, these materials suffer from wide band gap energies, as well as rapid $e^- - h^+$ recombination [16]. These drawbacks could be mitigated by combining the ZnO and MgO pure semiconductor materials to form a ZnO/MgO nanocomposite material, which should be investigated for MB photocatalytic degradation.

Optimizing the photocatalytic process is an essential step to maintain a feasible (reduced cost and time) wastewater treatment scheme [17]. Regression models could be used to predict the treatment system performance and optimize the operational factors. However, by increasing the system complexity and non-linearity (by adding more independent variables), the least squares optimization process could not deliver accurate outputs [3]. Moreover, the regression equations sometimes fail to yield the anticipated preciseness ability and predictability for describing the interactions among the input/output variables [18]. Alternatively, artificial neural network (ANN) has found successful applications in simulating the treatment of various wastewater sources using photocatalytic technology. An ANN is a non-linear prediction model that has a structure consisting of several interconnected processing elements, known as neurons [19]. The elements of this computational (black box) model are also recognized as units or nodes, and they are arranged in layers. Each neuron receives a number of weighted signals from the formerly linked nodes that are further combined and summed up to derive a certain response. This output represents either the last projected finding or an input attribute to the consequent phase, according to the layer ordering in the network topology [20]. A comparison between the product and the actual (target) values is then employed to adjust the network parameters (e.g., weights and biases), enhancing the prediction preciseness. The ANN models could be employed to capture inter-relationships among input and output data pairs that are unclear, nonlinear, or too hard to designate.

While several studies have focused on removing dyes from wastewater by photocatalytic degradation [6,8,21], there is still a research gap in optimizing the associated operational factors to maintain a techno-economically feasible process. Much effort should be exerted on employing artificial intelligence techniques to optimize the photocatalytic degradation process, aiming at minimizing the unit treatment costs. Hence, the current study focuses on creating and characterizing a smart ZnO/MgO nanocomposite material for MB photocatalytic degradation, followed by optimizing the photocatalytic process using ANN. This optimum condition is used to minimize the photocatalytic degradation price expressed by the capital and operational costs. This study's outputs could provide essential steps to find environmental and economic solutions for endorsing photocatalytic wastewater treatment under sustainable industrial-scale implementations.

2. Materials and Methods

2.1. Material Preparation

The ZnO and MgO nanoparticles were synthesized using a co-precipitation method, as previously reported (Figure 1; ref. [22]). The chemicals utilized throughout the study are tabulated in Supplementary Table S1. $\text{ZnSO}_4 \cdot 7\text{H}_2\text{O}$ and $\text{MgCl}_2 \cdot 6\text{H}_2\text{O}$ were used as precursors for ZnO and MgO. The 0.5 M solutions of the precursors were prepared in separate beakers. Under continuous stirring at 500 rpm, a 1 M solution of NaOH was added dropwise to each beaker until a white precipitate started to form. NaOH was added to maintain a pH of 12. Thereafter, stirring proceeded for about 15 min, allowing a complete precipitate formation. The ZnO and MgO precipitates were separated from the solution by filtration and washed multiple times with distilled water. The washed precipitates were then dried overnight at 105 °C. The dry material was crushed into fine powders, followed by calcination in a muffle furnace at 350 °C and 800 °C to achieve the ZnO and MgO nanopowders, respectively.

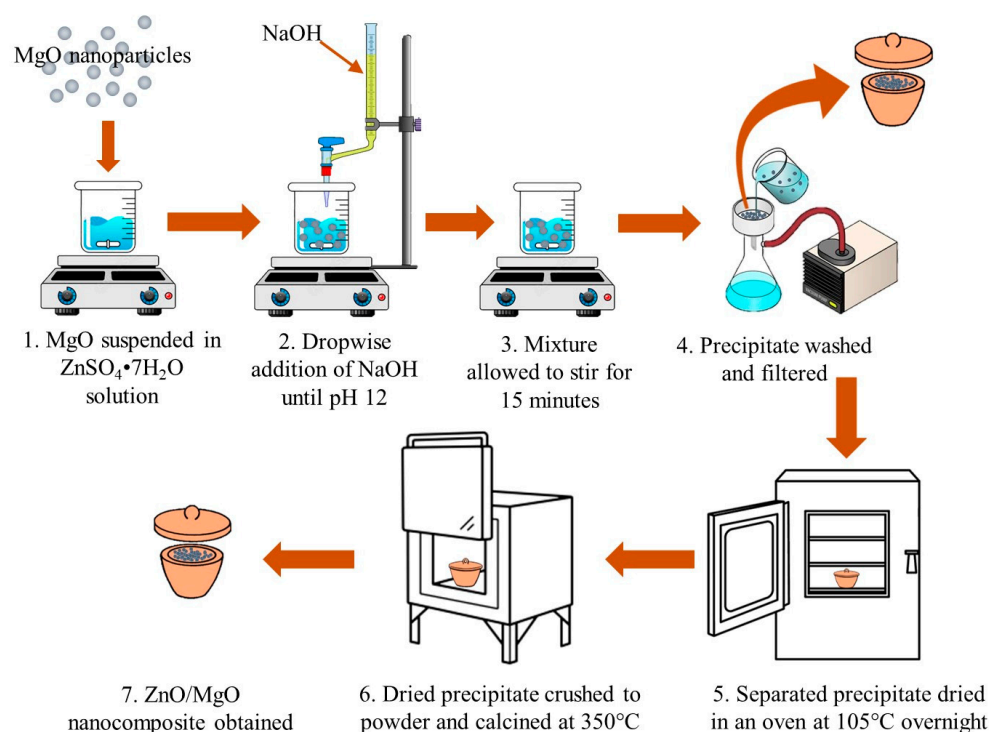


Figure 1. Synthesized technique of ZnO/MgO nanocomposite used for photodegradation of MB dye.

To synthesize the ZnO/MgO nanocomposite, an amount of already synthesized MgO was dispersed into a solution of $\text{ZnSO}_4 \cdot 7\text{H}_2\text{O}$ (100 mL) and mixed continuously for 5 min. Thereafter, a solution of 1 M NaOH was supplemented to the suspension dropwise until the final pH condition reached 12. The formed precipitate was then processed in the same way as ZnO, yielding the ZnO/MgO nanocomposite.

2.2. Experimental Setup and Design

The test was conducted in a rectangular reactor with a 1 m³ internal volume. The reactor had two metal halide lamps (light intensity 25,000 lx, 400 W), emitting 510 nm UV-vis light. In each experimental run, 100 mL of dye solution was inserted into a 250 mL beaker. A 2 mL sample was withdrawn, transferred through a 0.22 µm nylon syringe filter, and analyzed to obtain the MB concentration. The dye solution's pH was adjusted to the desired level using either H_2SO_4 or NaOH. The required amount of photocatalyst material was then supplemented to the aqueous medium. The beakers were inserted into the reactor and maintained under the dark condition (with mixing) to reach adsorption–desorption

equilibrium. Once the equilibrium was observed, another 2 mL sample was withdrawn, and the lamps were turned on and the photocatalytic reaction proceeded for the required period of time. After finishing each experimental run, 2 mL of the sample was again collected and filtered to discard the catalyst material before analysis.

Experimental design and parameter optimization were conducted using Design Expert Trial version 9 software, where a Box–Behnken design (BBD) represented the influence of four independent variables (i.e., catalyst dose, dye level, pH, and duration) on the MB removal efficiency (R%) as the response. Three levels of the input variables (−1, 0, +1) with four factors (Table 1) were used to generate the BBD matrix, giving a total of 29 experimental runs. The assigned ranges were selected based on primary results for MB photocatalytic degradation (see Supplementary Figure S1).

Table 1. Independent variable ranges used in the Box–Behnken design (BBD) experimental design to optimize methylene blue (MB) photocatalytic degradation by the as-prepared ZnO/MgO nanocomposite.

Variable Name	Symbol	Unit	Low	Mid	High
			Coded		
			−1	0	1
			Real Value		
Dye level	A	ppm	10	55	100
Catalyst dose	B	mg/L	100	550	1000
Medium pH	C	-	3	6.5	10
Period	D	min	60	120	180

After finishing the experimental runs, the photocatalysts were subjected to distilled water several times (washing) and then dried at 105 °C overnight to determine the regeneration and recyclability performance [23].

2.3. Analytical Analysis

The MB dye concentrations were detected using a UV spectrophotometer (Jasco V-630 spectrophotometer, Tokyo, Japan) adjusted at a wavelength of 664 nm. The medium pH was monitored using a pH meter (Model Lutron YK-2001 PH). X-ray diffraction (XRD) analysis (Shimadzu XRD-6100, Kyoto, Japan) with a Cu-K α radiation beam ($\lambda = 0.154$ nm) was carried out to obtain the crystallographic data of the synthesized photocatalysts before and after MB photodegradation. Fourier transform infrared spectroscopy (FTIR 8400s, Shimadzu, Kyoto, Japan) was applied to observe the photocatalyst's surface functional groups. The nanocrystalline nature, elemental composition, and surface morphology of the synthesized photocatalysts were given by a transmission electron microscope (TEM) equipped with energy dispersive X-ray spectrometer (EDS) (JEOL, JEM-2100F, Tokyo, Japan) and a scanning electron microscope (SEM) (JEOL, JSM-6360LA, Tokyo, Japan). The Brunauer–Emmett–Teller (BET) N₂ adsorption–desorption method was employed to identify the photocatalyst surface area and associated pore size and volume. The catalyst's optical band gap energy was determined using UV-Vis diffuse reflectance spectrum (UV-Vis DRS, Jasco v-570 spectrometer, Tokyo, Japan) analysis.

2.4. Mathematical and Computational Models

2.4.1. Quadratic Regression Equation

A second-order polynomial model (Equation (1)) was employed to study the correlation between the four variables and the MB R%:

$$y = \beta_0 + \sum_{i=1}^n \beta_i x_i + \sum_{i=1}^{n-1} \sum_{j=i+1}^n \beta_{ij} x_i x_j + \sum_{i=1}^n \beta_{ii} x_i^2 \quad (1)$$

where y is the response (dye removal efficiency, $R\%$); n represents the number of independent (input) parameters; β_0 is the model intercept; β_i , β_{ij} , and β_{ii} represent the first-order (linear) constant, squared, and interaction effects, respectively; and x is the associated independent variables

The model adequacy and significance were assessed via an analysis of variables (ANOVA). Moreover, the impact of each of the four independent variables on the generated model outputs was also assessed using ANOVA under a significance level of 0.05. The adequacy of the generated model (goodness-of-fit) was further validated using the coefficient of determination (R^2) value.

2.4.2. Artificial Neural Network (ANN) Schematic Description

In this investigation, a feed-forward ANN model was applied to estimate and forecast the MB $R\%$ using four inputs of photocatalysis experimental factors, i.e., initial MB concentration (C_0), catalyst dosage, pH, and time (Figure 2). Feed-forward was chosen due to its simplicity and widely known network type able to calculate the response directly through single propagation (a forward path) [19]. Furthermore, back-propagation is recognized as a well-organized and promising supervised learning algorithm applied to optimize the network weights. Multiple epoch numbers (iterations) are run to minimize the mean squared error (MSE) between the predicted output and desired vector, further adapting the network architecture. The number of observations (records) used to simulate the ANN model was distributed as 70% (training), 15% (verification), and 15% (testing). MSE was used as the objective function (i.e., the stopping criteria) to describe the magnitude of the gradient of performance for validation. The ANN-related calculations were carried out using MATLAB (R2015a) software.

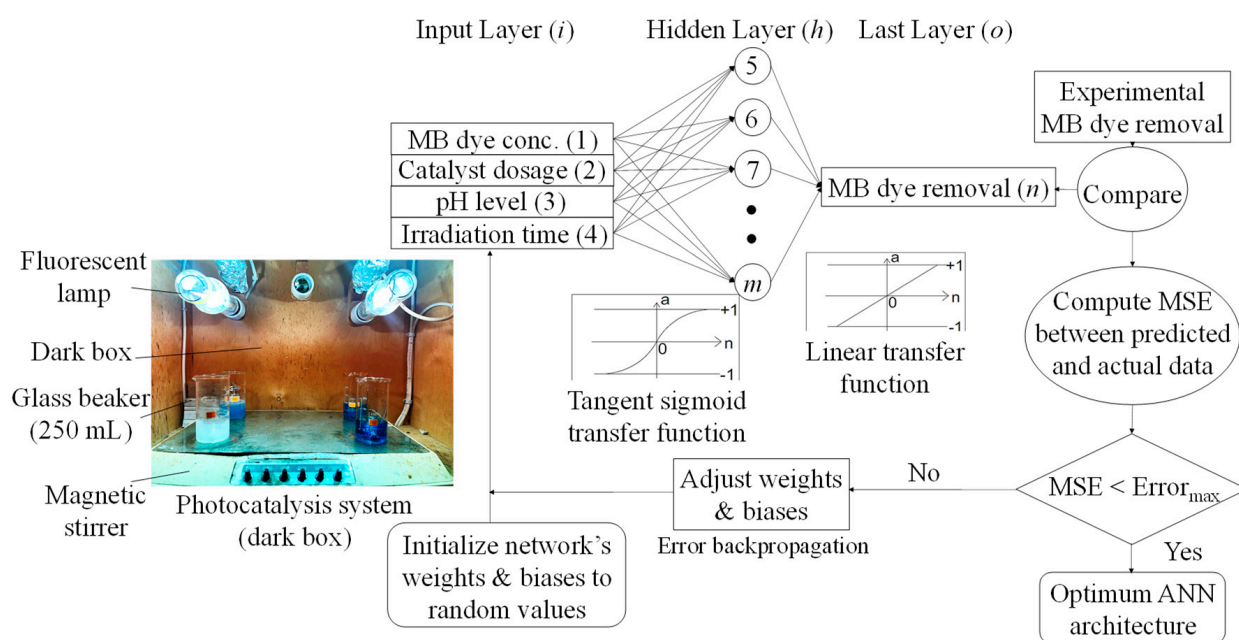


Figure 2. Schematic flowchart of ANN feed–forward back–propagation used to predict methylene blue (MB) removal efficiency under a photocatalytic degradation process.

3. Results and Discussion

3.1. Photocatalyst Characterization

The XRD, FTIR, SEM/EDS, TEM, BET, and UV-vis DRS characterization techniques were applied to the synthesized ZnO and MgO nanopowders, and the results were compared to those obtained from the ZnO/MgO nanocomposite.

3.1.1. XRD Characterization

Figure 3a shows the XRD diffraction profile of pure ZnO, defining peaks at 2θ of 31.6° , 34.3° , 36.1° , 47.5° , 56.5° , 62.7° , 66.2° , 67.8° , and 68.9° . These peaks could correspond to the crystal plane values of hexagonal pure ZnO (JCPDS ref. code 01-079-0207) given by (100), (002), (101), (102), (110), (103), (200), (112), and (201). These XRD peaks complied with those obtained for zinc oxide hollow spheres [24]. The XRD pattern (Figure 3a) also showed characteristic peaks of the cubic structure of pure MgO (JCPDS Ref code 01-074-1225). These peaks were observed at 2θ of 36.8° , 42.8° , 62.2° , 74.5° , and 78.5° , corresponding to the crystal plane values of pure cubic MgO given by (111), (200), (220), (311), and (222), respectively. The diffraction pattern generated complied with those obtained for periclase MgO in an AC-ZnO/MgO nanocomposite [9].

The diffraction pattern of the ZnO/MgO nanocomposite (Figure 3b) showed a combination of the characteristic peaks of hexagonal ZnO and cubic MgO structures. These peaks were denoted by 2θ at 31.8° , 34.1° , 36.1° , 37.8° , 42.6° , 47.5° , 56.4° , 62.1° , and 68.0° . This combination of peaks was indicative of a synergistic effect between ZnO and MgO to obtain the nanocomposite. The presence of extra peaks at 20.2° , 50.7° , and 58.5° could be due to some of the MgO being converted into $\text{Mg}(\text{OH})_2$ as a result of moisture adsorption during the synthesis process. These extra peaks corresponded to the (001), (102), and (110) crystal planes of $\text{Mg}(\text{OH})_2$ nanosheets [25].

The CIs of nanoparticles were calculated by Equation (2):

$$CI\% = \frac{A_c}{A_t} \times 100 \quad (2)$$

where A_c is the area under the crystalline peaks of the XRD pattern and A_t is the total area under the entire XRD pattern of a respective material

The CIs of ZnO and MgO were 67.04% and 60.83%, respectively. The core-shell nanocomposite had a higher CI of 71.92%. The crystalline size (D) of the synthesized catalyst materials was also calculated following the Debye-Scherrer equation (Equation (3)):

$$D = \frac{K\lambda}{\beta \cos \theta} \quad (3)$$

where K is the Scherrer constant representing the shape factor (assumed as 0.9), λ is the X-ray beam wavelength (1.541874 \AA), β is the full-width half-maximum value of a peak, and θ is the diffraction angle of each peak.

The crystalline size of ZnO was 22.99 nm, complying within the 11.84–24.82 nm range for ZnO synthesized under different pH conditions [26]. The estimated crystalline size of MgO (32.72 nm) obeyed that of MgO synthesized using a 1 M solution of precipitator [27]. Finally, the crystalline size was reduced to 17.24 nm for the synthesized nanocomposite material.

3.1.2. FTIR Characterization

The FTIR peaks observed at 3440.10 cm^{-1} in the three materials (Figure 3c) could correspond to the O–H stretching mode of the hydroxyl functional group [28]. The H–O–H stretching of H_2O could reflect the high affinity of MgO to adsorb water molecules. The peaks detected at 1643.65 cm^{-1} and 1135.76 cm^{-1} were attributed to the O–H stretch vibration [29]. A peak at 1430.05 cm^{-1} was also noticed, indicating the bending vibrations of H_2O adsorbed onto the catalyst material surface [30]. The peaks in the region below 700 cm^{-1} could identify the metal–oxygen bonds [31], e.g., the peaks at 681.21 cm^{-1} and 591.67 cm^{-1} represented the Mg–O bond, and the peak at 424.57 cm^{-1} denoted the Zn–O bond. The presence of these peaks further verified the successful combination of ZnO and MgO.

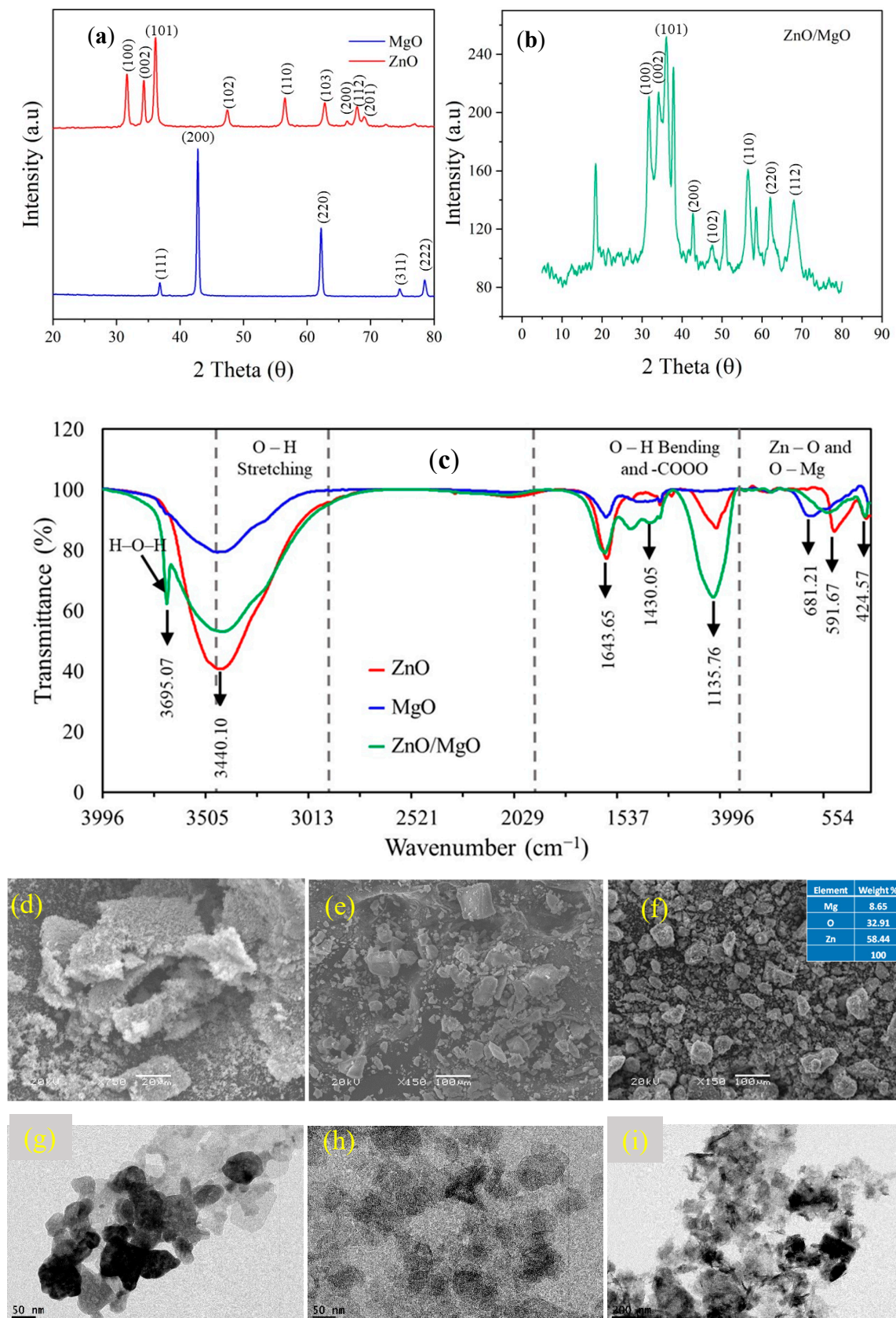


Figure 3. Characterization of synthesized nanocomposites. (a) XRD peaks of ZnO and MgO, (b) XRD peaks of ZnO/MgO, (c) FTIR spectra, (d) SEM of ZnO, (e) SEM of MgO, (f) SEM of ZnO/MgO, (g) TEM of ZnO, (h) TEM of MgO, and (i) TEM of ZnO/MgO.

3.1.3. SEM/EDS Characterization

The SEM micrograph of pure ZnO (Figure 3d) showed a spongy appearance of agglomerated particles. This result was similar to that obtained for ZnO synthesized via the precipitation technique [32]. The SEM micrograph of pure MgO displayed flat plate-like structures (Figure 3e) of varying sizes. A similar structure was obtained for MgO by employing the co-precipitation method [33]. The SEM micrograph of the ZnO/MgO nanocomposite (Figure 3f) showed a rough external surface that appeared to be a coating of ZnO over MgO. This surface roughness might be due to the gathering and building up of numerous small clusters of ZnO that coated the MgO core nanoparticles. The EDS results showed that Zn had the highest percentage weight followed by Mg and O. This result further verified the successful synthesis of the nanocomposite material, where the ZnO nanoparticles were deposited on MgO (the support material).

3.1.4. TEM Characterization

The TEM image showed that the ZnO particles were irregularly shaped and mildly varied in size (Figure 3g). The agglomeration of ZnO could occur due to the exclusion of capping agents during the particle synthesis process. The TEM image of MgO depicted the existence of roughly circular plate-like structures of a relatively uniform size (Figure 3h). Finally, the TEM image of the ZnO/MgO nanocomposite showed a mixed matrix of the plate-like MgO particles surrounded by the spongy appearance of the ZnO particles (Figure 3i). This result further confirmed that the ZnO/MgO nanocomposite was successfully synthesized, complying with the SEM observations. The particle sizes were measured using Image J free version 1.53t software, revealing 62.96 nm for ZnO, 77.27 nm for MgO, and 114.5 nm for ZnO/MgO.

3.1.5. BET Characterization

The BET analysis exhibited the material N₂ adsorption–desorption isotherms, complying with the existence of mesoporous surfaces (see Supplementary Figure S2a–c). The isotherm shapes of MgO and ZnO fit the type IVb isotherm, whereas the ZnO/MgO nanocomposite shape matched the type IVa isotherm. This finding revealed the presence of a type H3 hysteresis loop, probably depicting the existence of ≥ 4 nm diameter pores. Further, the BET analysis indicated a substantial decrease in the MgO surface area from 80.756 to 30.536 m²/g after combination with ZnO (Table 2). This finding could be ascribed to the formation of more pores on the ZnO/MgO surface, where interparticle spaces were formed due to the growth of ZnO particles on the MgO surface, as previously reported [34]. This result was further confirmed by the significant increase in the pore diameter from 4.942 nm for MgO to 26.617 nm for ZnO/MgO (Table 2). The pore volumes were also measured; it was observed that the ZnO/MgO nanocomposite possessed the largest pore volume of 0.529 cm³/g.

Table 2. Summary of BET analysis results for ZnO, MgO, and ZnO/MgO catalyst materials.

Catalyst Material	BET Pore Diameter (nm)	BET Surface Area (m ² /g)	BET Pore Volume (cm ³ /g)
ZnO	7.752	11.183	0.021
MgO	4.942	80.756	0.109
ZnO/MgO	26.617	30.536	0.529

3.1.6. UV-Vis DRS Characterization

Figure 4a–c shows the indirect Tauc plots and absorbance curves of the synthesized nanomaterial. The indirect Tauc plots were generated by Equation (4) [35]:

$$(F(R)hv)^n = A(hv - E_g) \quad (4)$$

where $F(R)$ is the Kubelka–Munk function, A is a proportionality constant, $h\nu$ is the incident photon energy, $n = \frac{1}{2}$, and E_g is the band-gap energy

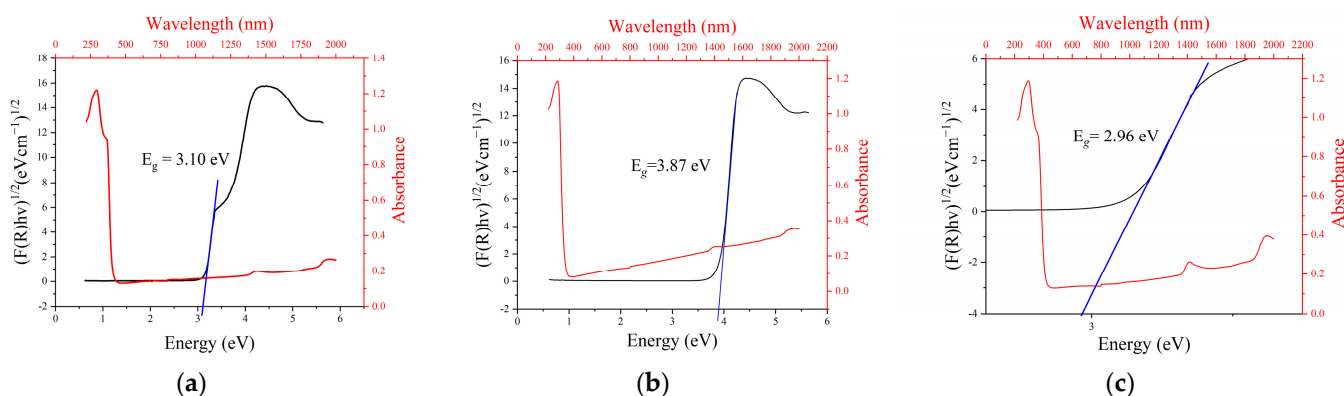


Figure 4. Energy band gaps of (a) ZnO, (b) MgO, and (c) ZnO/MgO nanocomposites.

The linear section of the Tauc plot was extrapolated, cutting the x -axis at the energy band gap value. The UV-vis DRS results showed that the optical band gap energies of ZnO, MgO, and ZnO/MgO nanomaterials were 3.10, 3.87, and 2.96 eV, respectively. This implies that the energy band gap was successfully reduced following the combination of ZnO and MgO. This reduced energy band gap of the nanocomposite could facilitate photocatalytic activity under UV light with a wavelength of ≈ 419 nm, obeying the visible light range.

3.2. Regression Model Application for Predicting MB Removal

The second-order polynomial regression model, governing the R% due to the interactions of the four independent variables, was generated (Equation (5)):

$$R\% = 56.342 - 1.084A - 0.02466B + 4.978C - 0.473D - 6.1 \times 10^{-5}AB - 0.1019AC + 4.35 \times 10^{-4}AD + 3.843 \times 10^{-3}BC + 4.402 \times 10^{-6}BD + 0.0465CD + 9.744 \times 10^{-3}A^2 + 9.362 \times 10^{-6}B^2 - 0.2177C^2 + 8.92 \times 10^{-4}D^2 \quad (5)$$

where R% is the MB removal efficiency (%); and the variables A, B, C, and D represent the dye level (ppm), catalyst dosage (mg/L), solution pH, and period (min), respectively.

An ANOVA test was performed to assess the accuracy and adequacy of the model generated (Table 3). The quadratic model exhibited an F -value and a p -value of 70.33 and <0.0001 , respectively. The derived F -value was greater than the recognized F -value of 2.352 (at 95% significance) [18], signifying the model's appropriateness to forecast the R% observations. Moreover, these statistical results verified that the model was significant, where the p -value was below the alpha significance level. The model's prediction accuracy was also demonstrated by the predicted and adjusted R^2 values (0.9195 and 0.9720, respectively). These R^2 values were relatively high and the difference between them was less than 0.2, denoting that the data and the model were appropriately chosen and suitable for estimating the R% values [17]. Moreover, the R^2 value of the model was relatively high, presenting a value of 0.9860. Based on these statistical indicators, the generated quadratic equation could give acceptable predictions of the R% values, i.e., the predicted removal efficiencies were in agreement with the actual measurements (see Supplementary Figure S3). The significance of the variables was also analyzed, giving a p -value for each of A, B, C, and D below 0.05.

3.3. Artificial Neural Network (ANN) Application for Predicting MB Removal

3.3.1. Determining the Optimum ANN Architecture

The neurons' number in the hidden layer (N) was altered to examine the ANN prediction performance, evaluating the R^2 values and MSE of each ANN architecture (see Supplementary Table S2). It was noticed that increasing N enhanced the model prediction

criterion during and after training. As such, the deficient N caused premature convergence or early termination of the training algorithm, hindering the network learning capability. The N = 8 established the best-hidden neuron arrangement, giving the smallest MSE of 11.20 and the highest R^2 of 0.9464 (see Supplementary Table S2). However, a further increase in N raised the model MSE, resulting in poor network generalization. An excessive N prolonged the calculation period (causing extra fitted functions due to the complex structure), and the training phase became probably accompanied by local minima or over-fitting. Over-fit (or over-learn) represented the network condition that maintained a smaller MSE (e.g., better R^2) for the training procedure, but the test procedure suffered from lower R^2 performances. This optimum N was accompanied by choosing Levenberg–Marquardt (*trainlm*) as the training function. As such, the Levenberg–Marquardt algorithm was highly efficient in simulating complex relationships among input variables within reasonable computation times. Moreover, this learning function is suitable for training moderate-sized feed-forward ANN models and solving nonlinear least squares problems. Hence, a three-layer feed-forward back-propagation ANN, with a “*trainlm*” training function and a “4–8–1” topology to forecast the MB R(%), was selected.

Table 3. Analysis of variables (ANOVA) for prediction of photocatalytic methylene blue (MB) removal by ZnO/MgO nanocomposite using four independent variables, namely initial MB concentration (A), catalyst dosage (B), aqueous solution pH (C), and time (D). The model accuracy is given by R^2 0.9860; adjusted R^2 0.9720; predicted R^2 0.9195; Adeq precision 31.8040.

Source	Sum of Squares	df	Mean Square	F-Value	p-Value	Significance
Model	17,842.80	14	1274.49	70.33	<0.0001	significant
A	10,467.64	1	10,467.64	577.61	<0.0001	significant
B	147.40	1	147.40	8.13	0.0128	significant
C	2640.01	1	2640.01	145.68	<0.0001	significant
D	208.60	1	208.60	11.51	0.0044	significant
AB	6.11	1	6.11	0.3371	0.5707	insignificant
AC	1030.82	1	1030.82	56.88	<0.0001	significant
AD	5.52	1	5.52	0.3043	0.5899	insignificant
BC	146.57	1	146.57	8.09	0.0130	significant
BD	0.0565	1	0.0565	0.0031	0.9563	insignificant
CD	381.66	1	381.66	21.06	0.0004	significant
A ²	2525.61	1	2525.61	139.36	<0.0001	significant
B ²	23.31	1	23.31	1.29	0.2758	insignificant
C ²	46.14	1	46.14	2.55	0.1329	insignificant
D ²	66.90	1	66.90	3.69	0.0753	significant

3.3.2. Training and Validation Performances

The MSE values were plotted against the epoch numbers (Figure 5a). In this diagram, the simulation procedure was completed by either achieving the highest number of training trials (e.g., training termination after six epochs) or reaching the smallest MSE (e.g., $MSE = 10^{-6}$ as a performance goal), whichever initially ensued [36]. The training phase MSE (performance function) considerably dropped with iteration counts, reflecting the network’s capability to modify its weights and biases until reaching the third epoch. After that point, the training curve MSE remained approximately unchanged, depicting the ANN model’s ability to learn the relationships between the input and output data pairs. The validation set showed a different behavior, where its MSE curve increased until the first epoch and then remained almost constant. For instance, the best validation profile was monitored at epoch 0 with an MSE of 11.2, after which the ANN model initiated to overfit the data and lose its generalization power (Figure 5b). The MSE of the testing step increased, approximately similar to that of validation, employing that the learning step generated excess parameters. Hence, the zero epoch was used to terminate the training process, ensuring that the network model could precisely forecast R% using unseen input data.

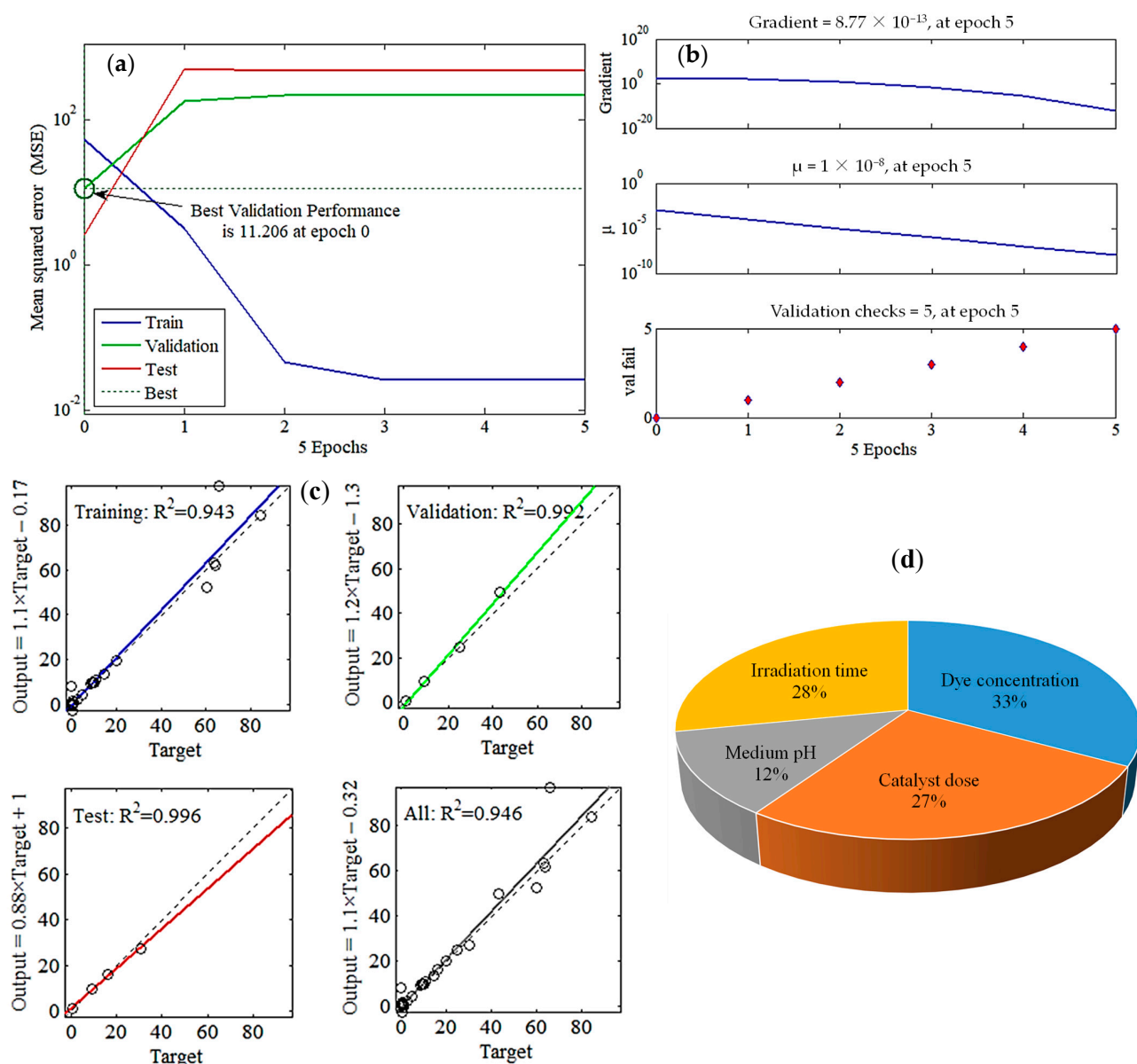


Figure 5. ANN (4-8-1) model employed to predict methylene blue (MB) removal efficiency using four inputs, namely MB concentration, catalyst dosage, pH, and time. (a) Training state, (b) validation performance, (c) regression data, and (d) sensitivity analysis.

3.3.3. Optimum Weights and Biases

At epoch = 0, the ANN model was well-learned and the network parameters (i.e., weights and biases) were adequately adapted (see Supplementary Table S3). The values of the linking weights ($W_{8 \times 4}$ and $W_{1 \times 8}$) and bias levels ($B_{8 \times 1}$ and $B_{1 \times 1}$) were determined based on the *trainlm* optimization algorithm. The layer outputs used to predict R% that matched the target (the best cross-validation performance) were calculated as follows:

Each parameter (independent variables) in the four-dimension input layer ($P_{4 \times 1}$ vector) was multiplied by its corresponding record in the weight matrix, $W_{8 \times 4}$, and then cumulated. Then, an eight-dimension bias, $B_{8 \times 1}$, was included, and a hyperbolic tangent sigmoid “*tansig*” activation function was used to transform the net input into a response signal ($z_{8 \times 1}$) (Equation (6)):

$$z_{8 \times 1} = \text{tansig} \left(\sum (W_{8 \times 4} \cdot P_{4 \times 1}) + B_{8 \times 1} \right) \quad (6)$$

The products of the eight-dimension middle layer, $z_{8 \times 1}$, were weighted and integrated into the matrix, $W_{1 \times 8}$, and, further, a one-dimension bias ($B_{1 \times 1}$) was included. The last output was introduced to a linear “purelin” activation function, yielding the last layer correlation (Equation (7)):

$$y_{1 \times 1} = \text{tansig}(\sum(W_{1 \times 8} \cdot z_{8 \times 1}) + B_{1 \times 1}) \quad (7)$$

3.3.4. Regression Plot

Figure 5c displays the schemes of the simulated MB (R%) by ANN against their associated experimental data, along with R^2 values of training, validation, and testing. In each regression sub-plot, the solid line denotes the best match of the ANN model. The dashed line represents the model outputs that fit precisely the actual observations (i.e., the theoretical fitting condition with $R^2 = 1.000$). An overall R^2 of 0.946 designated that the developed ANN (4–8–1) model could explain up to $\approx 95\%$ of the variability in the MB removal data.

3.3.5. Relative Importance

The obtained weights and biases (see Supplementary Table S3) were involved in computing the relative importance (RI) of the experimental parameters, following Garson’s formula [37]. Figure 5d shows that the RI for the dye concentration reached its maximum value at 33%, followed by irradiation time (28%), catalyst dosage (27%), and finally the medium pH (12%). Moreover, the RI values depicted that the investigated independent variables were important for improving the MB photocatalytic degradation performance.

3.4. Photocatalysis Operating Factors Optimization

The created ANN model was considered as the fitness function and combined with a genetic algorithm (GA) to optimize the photocatalytic experimental factors. The assigned GA had 100 iteration numbers, 10 population size, 0.4 crossover probability, and 0.2 mutation probability, and was required to maintain R(%) greater than 90%. This procedure depicted that, at $C_0 = 16.42$ mg/L and pH = 9.95, the catalyst dosage and time could be 905 mg/L and 174 min, respectively. These values were estimated as 907.35 mg/L and 178 min, respectively, using the quadratic model optimization procedure (see Supplementary Figure S4). Operating the photocatalytic reactor under the ANN-based optimized factors maintained a shorter reaction time and a lower oxidant level compared with the quadratic model-based optimized factors.

According to the verification experiment conducted under the optimum condition, the absolute relative deviation between the ANN model outputs and experimental data was 1.70%, which was smaller than 4.54% for the quadratic model prediction performance. A better predictive accuracy of ANN could be assigned to its universal ability to capture and approximate the non-linearity of the photocatalytic system, whereas the regression model is only limited to second-order polynomial.

3.5. Effect of Independent Variables on MB Degradation

The MB removal efficiencies (R%) were highly influenced by varying the independent variables within the experimental range (Figure 6):

3.5.1. Effect of Initial MB Concentration

Increasing the C_0 within the 10–100 mg/L range was noticed to reduce the R% observations (Figure 6). This decrease in R% could be because of the blocking of active sites available on the nanomaterial surface by a surplus of MB molecules [21]. This pattern was associated with an ineffective photon–catalyst interaction, where a portion of photon energy could be absorbed by the MB molecules rather than by the catalyst phase. This action reduced ROS generation (higher MB:ROS ratios); i.e., there would be an insufficient ROS amount to degrade the MB in the aqueous solution. Another reason for R% reduction

at higher C_0 could be the hindering of light penetration through the dye solution and to the photocatalyst surface [12].

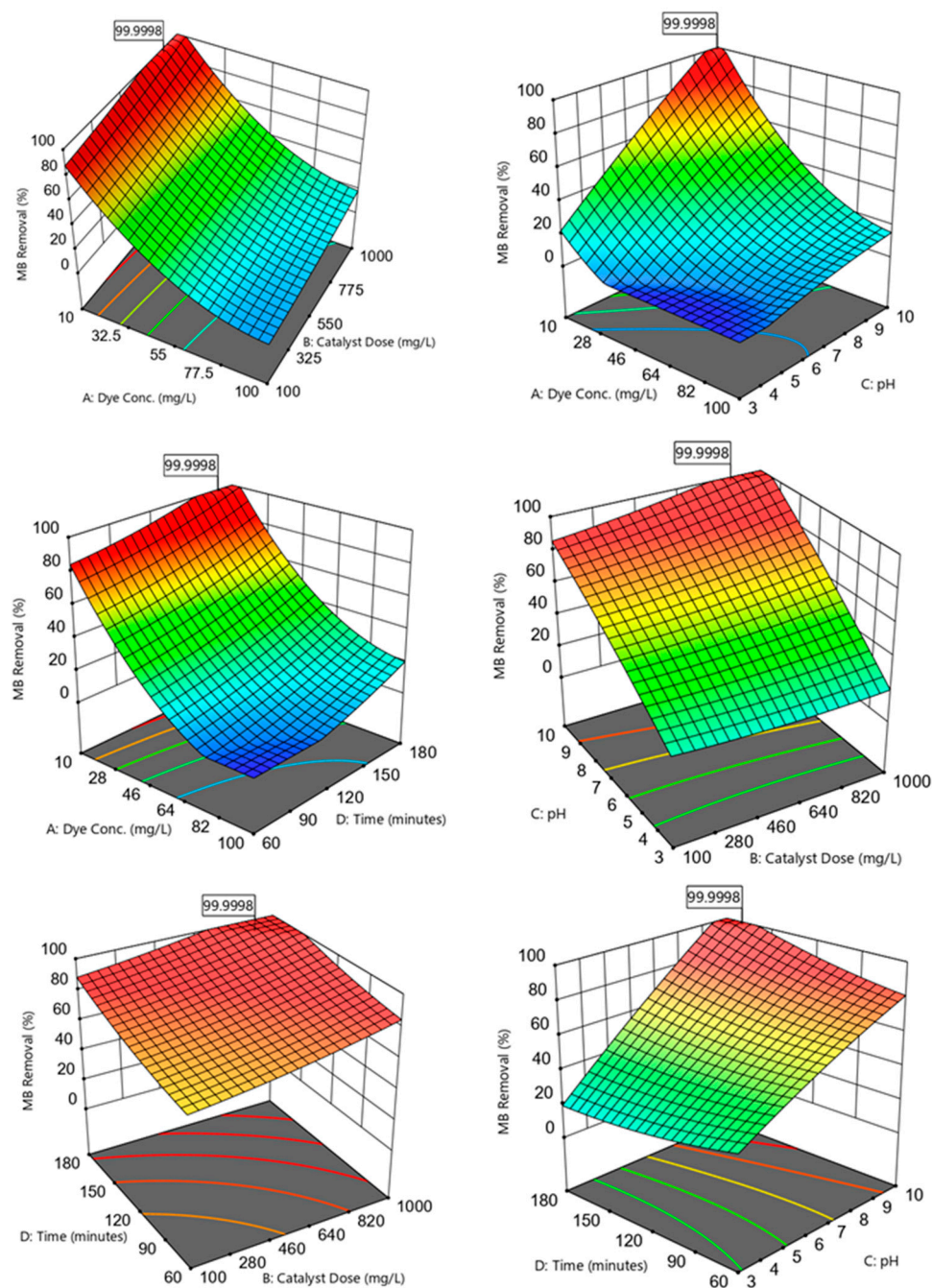


Figure 6. Three-dimensional plots showing the correlations between the MB removal efficiencies and the independent variables; dye concentration, catalyst dose, pH, and photodegradation time.

3.5.2. Effect of Catalyst Dose

The analysis showed that the MB R% was gradually improved by increasing the photocatalyst dosage within the 100–1000 mg/L range (Figure 6). This enhanced performance could be ascribed to an increase in the active site amounts when a high catalyst dosage was introduced to the medium [38]. These active locations could absorb more photons for maintaining the photocatalytic reactions. Increasing the available active sites facilitated the active site–photon interactions, yielding surplus ROS to degrade the MB dye [21].

3.5.3. Effect of pH

The results revealed an improved photocatalytic performance by increasing the solution pH within the 3–10 range (Figure 6). Varying the medium pH directly influenced the photocatalyst surface charge and the associated attraction and repulsion forces between the catalyst and the dye. The catalyst surface could acquire more negative charges as the medium pH became greater than the point of zero charge (pH pzc). Accordingly, as the medium pH became closer to the pH pzc of ≈ 10.24 , the negatively charged sites tended to form strong attraction forces with the cationic MB molecules. When the catalyst was supplemented with the MB solution, it was recognized that the pH would increase to values greater than the initial pH. Increased attraction of the MB onto the photocatalyst surface resulted in better MB–ROS interactions and higher MB degradation efficiencies. Moreover, higher pH values implied the presence of more OH^- present in the solution, resulting in the formation of more $\bullet\text{OH}$ radicals to degrade MB [2]. The medium pH could also affect the MB dye dissociation pathway. For instance, the MB dye tended to be ionized and possessed a predominantly cationic species (positive charge) at a solution pH over 3.8 (i.e., the MB dissociation constant, pKa) [39].

3.5.4. Effect of Irradiation Time

The proportional relationship between the irradiation time (60–180 min; Figure 6) and MB R% could be denoted by the prolonged interactions between the dye molecules and the ROS available on the photocatalyst surface [40]. The adsorption of MB onto the material surface could be designated as a function of time until active sites' occupation and saturation, restricting the diffusion mobility of photocatalytic electrons [6].

3.6. Recyclability of the Photocatalyst Material

A recyclability test was performed to investigate the photocatalytic performance of the as-prepared materials for multiple regeneration and reuse cycles (see Supplementary Figure S5). After six successive cycles, the ZnO/MgO nanocomposite exhibited a minor drop in MB removal of about 6.14% compared with 10.56% for ZnO and 13.39% for MgO. It was supposed that ZnO/MgO exhibited higher stability and regeneration capacity than ZnO and MgO individually. However, this photocatalytic efficiency became insufficient in increasing the number of cycles above six. This reduction in performance could be ascribed to the photocatalyst mass loss after repeated use and/or the blocking of active sites by dye traces. This stability was better than B–N–TiO₂/EP photocatalyst material, which showed a reduction in performance >10% for dye degradation after five cycles [41].

3.7. Photocatalytic Degradation Rates and Suggested Degradation Mechanisms

The data in Figure 7a denoted that the MB photocatalytic degradation data fit the pseudo-first order kinetic model [42] with a high R^2 range of 0.957–0.992. The study also depicted that the degradation rate constant was 0.025 min^{-1} for ZnO/MgO. This rate constant was considerably greater than that observed for ZnO (0.003 min^{-1}) and MgO (0.0014 min^{-1}). In particular, this degradation kinetic investigation verified the superiority of the ZnO/MgO nanocomposite for the photocatalytic degradation of MB.

Figure 7b shows the photocatalytic degradation mechanism related to the ZnO/MgO nanocomposite. The conduction and valence band energies of ZnO and MgO were calculated using the equations given by Equations (8) and (9) [43]:

$$E_{CB} = X - E - 0.5E_g \quad (8)$$

$$E_{VB} = E_{CB} + E_g \quad (9)$$

where E_{CB} = conduction band energy; E_{VB} = valence band energy; X = electronegativity value; E = electron energy on the hydrogen scale; E_g = band gap energy.

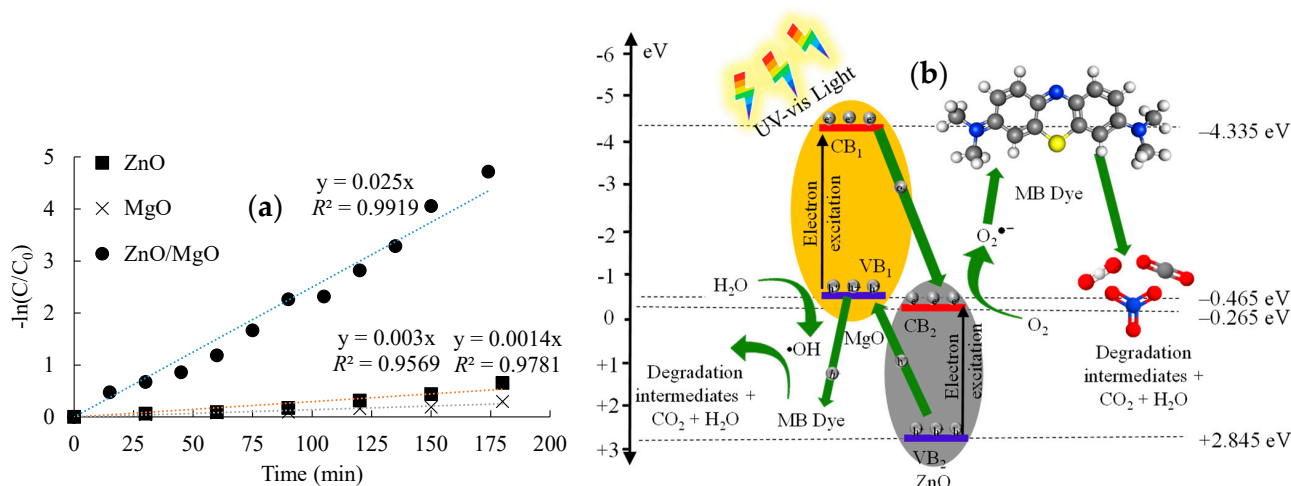
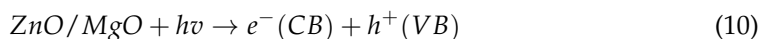


Figure 7. Photocatalytic degradation of MB dye. (a) Pseudo—first order fitting and (b) suggested degradation mechanisms.

The E_{CB} and E_{VB} of ZnO were determined as -0.265 eV and $+2.845$ eV, respectively, whereas the E_{CB} and E_{VB} of MgO were calculated as -4.335 eV and -0.465 eV, respectively. The CB and VB values were then used to derive the proposed MB degradation mechanism (Figure 7b). When the ZnO/MgO nanocomposite was exposed to light irradiation, the photocatalytic reaction governed by Equation (10) would occur to generate e^- and h^+ :



where $e^-(CB)$ = electrons in the conduction band; $h^+(VB)$ = the electron vacancy in the valence band.

The VB electrons would absorb photon energy and jump into the CBs. The band energy of the ZnO CB possessed a more positive potential than the VB of MgO. Consequently, the photogenerated e^- in the CB of MgO would have a stronger affinity to migrate and accumulate in the CB of ZnO instead of recombining with the holes in the MgO VB. Simultaneously, the h^+ left in the VB of ZnO would migrate and accumulate in the more negative VB of MgO. This charge transfer tended to reduce the e^-/h^+ recombination, resulting in enhanced photocatalytic activity of the ZnO/MgO nanocomposite.

Following the charge transfer process, the e^- and h^+ accumulated in the ZnO CB and MgO VB, respectively, would be free to interact with molecules in the surrounding MB solution. Electrons would reduce molecular oxygen (O_2) to create superoxide radicals ($O_2^{\bullet-}$), following Equation (11):

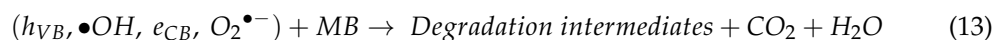


This reduction of O_2 could occur because the CB of ZnO possessed a sufficient reduction energy potential (more positive) to facilitate its conversion into $O_2^{\bullet-}$, requiring a reduction energy potential of -0.33 eV [44]. Simultaneously, the h^+ accumulated in the MgO VB would oxidize H_2O molecules present in the MB solution to form hydroxyl radicals ($\bullet OH$), following Equation (12):



This reaction could occur because the VB of MgO possessed a sufficient oxidation potential (more negative) to facilitate the conversion of H_2O to $\bullet OH$, which required a reduction potential of about $+1.9$ eV [45]. The ROS generated ($O_2^{\bullet-}$ and $\bullet OH$) would easily interact with MB molecules (Equation (13)), breaking it down into less toxic and simpler intermediates and eventually CO_2 and H_2O . Moreover, the photogenerated h^+

and e^- accumulated on MgO VB and ZnO CB, respectively, could directly interact with MB molecules:



3.8. Photocatalytic Degradation of MB Reported in the Literature

The effectiveness of the ZnO/MgO nanomaterial was compared with other ZnO- and MgO-based photocatalyst materials for MB dye removal (Table 4). Other photocatalysts have exhibited greater degradation performances at lower MB levels [24,31,46,47] and/or longer degradation times [48]. Most studies integrated ZnO and MgO into a third material, resulting in ternary photocatalysts [9,48] for improved performance. In our investigation, the photocatalyst material comprised ZnO and MgO, and the operational factors were optimized to obtain high degradation efficiencies for relatively higher dye concentrations. The results obtained in our study showed that the synthesized nanocomposite material could be successfully utilized for MB degradation.

Table 4. Comparison of the performance of the ZnO/MgO nanocomposite with other photocatalysts toward methylene blue (MB) removal.

Photocatalyst	Experimental Condition				Removal Efficiency (%)	Ref.
	MB Conc. (mg/L)	Catalyst Dose (mg/L)	pH	Time (min)		
ZnO/MgO nanocomposite	16.42	907.35	9.95	178	99.99	This study
ZnO/MgO/AC nanoparticle	3.2	1000	7	20	100	Karimi et al. [9]
Novel tri-phase CuO–MgO–ZnO nanocomposite	5	400	7	100	88.5	Munawar et al. [31]
ZnO/MgO nanocomposites	10	40	7	120	89.5	Panchal et al. [47]
Hollow MgO–ZnO microspheres	5	300	7	150	100	Vishwanathan et al. [24]
Ternary MgO/ZnO/In ₂ O ₃	10	500	7	300	98	Xiang et al. [48]
CdO–ZnO–MgO nanocomposite	1	25	7	120	91	Revathi and Karthik [46]

3.9. Economic Feasibility of the ZnO/MgO Nanocomposite Photocatalysis System

A cost-benefit analysis was performed to evaluate the economic feasibility of applying the ZnO/MgO nanocomposite for treating dye-polluted water. The optimum conditions obtained from the optimization of independent variables were utilized to design the photocatalytic system used in the analysis. The photocatalytic system was designed to treat a daily influent volume of 10 m³. This flow rate is suitable for a compact-sized wastewater treatment facility with simple equipment. The breakdown of the economic analysis comprised estimates of the capital/investment costs and operational/running costs (Table 5). These calculations were derived using a precision of $\pm 20\%$ [49], because cost estimation from the real-world application of photocatalysis could vary among countries based on the fluctuations in the currency exchange rates, assumptions applied, feed-in tariffs, and electricity demand. The preciseness and uncertainty of this economic estimation were also assessed by developing sensitivity analysis, varying the photocatalytic reactor cost, chemical prices, and electrical and water consumption costs between -30% and 30% [50] (see Supplementary Figure S6).

3.9.1. Capital Costs

The one-time expenses incurred to implement the photocatalysis system were represented by the capital costs. About 11.69% of these capital costs accounted for the pho-

photocatalytic reactor and tank installations, where the volume (V_c) could be estimated by Equation (14) [20]:

$$V_c = \frac{Q}{D} \times \frac{t_t}{t_w} \quad (14)$$

where Q represents the average volume of wastewater treated annually (m^3/yr), D is the number of working days per year (assuming 300 days per year), t_t is the optimum reaction time (e.g., 90 min), and t_w is the number of plant operation hours per day (e.g., 1440 min/d represents a 24 h daily plant operation time).

The obtained tank volume was then applied to calculate the construction cost by Equation (15) [51]:

$$CC = V_c \times C_p \quad (15)$$

where C_p represents the price per m^3 of a photoreactor unit derived from subcontractor and supplier quotes.

The cost of water collection tanks was also added to the initial investment. Moreover, the prices of mechanical equipment, comprising UV lamps (light source), a stirrer motor, pumps, and a rotary calcination furnace for catalyst synthesis, were also included, as previously reported [52].

Table 5. Cost estimates for the photocatalytic degradation of MB dye-laden wastewater ($10 \text{ m}^3/\text{day}$) using the ZnO/MgO nanocomposite under unoptimized and ANN-optimized conditions (using a precision of $\pm 20\%$).

Item	Cost		Justification
	Unoptimized	ANN-Optimized	
Photocatalysis installation (PI)	USD 15,500	USD 14,060	Reactors ($\text{USD } 1680 \times 2 = \text{USD } 3360$), UV lamps ($\text{USD } 1150 \times 2 = \text{USD } 2300$), stirrer motors ($\text{USD } 590 \times 2 = \text{USD } 1180$), pumps ($\text{USD } 2010 \times 2 = \text{USD } 4020$), and rotary calcination furnace ($\text{USD } 3200$). Optimized reaction time reduced the reactor volume by $\sim 6\%$
Piping, valves, and wiring	USD 4650	USD 4218	0.3 PI
Site work	USD 1550	USD 1406	0.1 PI
Subtotal (1)	USD 21,700	USD 19,684	1.4 PI = Q
Contractor O&P	USD 3255	USD 2953	0.15 Q
Subtotal (2)	USD 24,955	USD 22,637	1.15 Q = R
Engineering fees	USD 3743	USD 3395	0.15 R
Subtotal (3)	USD 28,698	USD 26,032	1.15 R = S
Contingency fees	USD 5740	USD 5206	0.2 S
Subtotal (4)	USD 34,438	USD 31,239	1.2 S = T
Others	USD 6888	USD 6248	0.2 T
Total capital cost	USD 41,325	USD 37,486	1.2 T
Annual capital cost	USD 8265/yr	USD 7497/yr	USD 37,486/project lifetime (5 yr)
Interest rate consideration	USD 10,056/yr	USD 9122/yr	USD 7497/yr $\times (1 + i)^n$
Unit capital cost	USD 3.35/ m^3	USD 3.04/ m^3	USD 9122/yr $\div (10 \text{ m}^3/\text{d} \times 300 \text{ d/yr})$
Chemical costs	USD 90/month	USD 75/month	15 kg/month \times USD 5/kg
Electrical consumption costs	USD 1157/month	USD 1105/month	8500 kWh/month \times USD 0.13/kWh
Water consumption	USD 42/month	USD 40/month	168 $\text{m}^3/\text{month} \times$ USD 0.24/ m^3
Labor cost	USD 120/month	USD 120/month	
Land rental costs	USD 42/month	USD 38/month	5% of total capital cost
Repair and maintenance costs	USD 126/month	USD 114/month	15% of total capital cost
Others	USD 168/month	USD 152/month	20% of total capital cost
Total operating cost	USD 1744/month	USD 1644/month	Sum of total operating items
Unit total operating cost	USD 5.81/ m^3	USD 5.48/ m^3	USD 1644/month $\div (10 \text{ m}^3/\text{d} \times 30 \text{ d/month})$
Unit total cost	USD 9.17/ m^3	USD 8.52/ m^3	Unit capital cost + Unit total operating cost

3.9.2. Operational Costs

The daily expenses incurred to run the photocatalysis system were represented by the operational costs. These costs included several items related to consumables, electricity consumption, salaries and wages, overheads, and plant maintenance [53]. The costs of

chemicals needed to synthesize and apply the ZnO/MgO nanocomposite were estimated by Equation (16):

$$Cost_{chemicals} = C_i \times P_i \quad (16)$$

where $Cost_{chemicals}$ is the monthly cost of chemicals incurred (USD/month), C_i is the quantity of chemicals supplied (kg/month), and P_i is the chemical price per unit weight (USD/kg)

The electricity utilization costs comprised the power consumption to operate an electronic overhead stirrer (69 W), pumps (55 W), and UV lamps (46 W) [54]. This amount of energy was used to estimate the electrical energy per order (E_{EO}) by Equation (17) [55]:

$$E_{EO} = \frac{38.4 \times P}{V \times k} \quad (17)$$

where P is the power of all electrical equipment (using 170 W), V is the volume of treated water per day (L), and k is the reaction rate constant ($\ln(C/C_0)$).

The consumption per m^3 (E_{EO}) was used to estimate the annual consumption for the plant receiving $10 m^3/day$. The annual consumption in KWh and the electricity feed-in tariff (USD 0.13/kWh) were then used to estimate the electricity consumption cost per year.

The costs of water required for photocatalyst synthesis and regeneration were also considered. This estimate was derived from the lab-scale preparation procedures, where ≈ 1 L of water was required to synthesize and regenerate 1 g of the ZnO/MgO nanocomposite. The water tariff was set at USD 0.24/ m^3 .

The costs associated with the repair and maintenance of the treatment system were estimated at 1.5% of all capital costs [51]. An employee salary rate of USD 120/month was utilized to determine the labor costs associated with water sampling (three samples/week), cleaning and repair of equipment, and operation of the photocatalysis system. Statutory obligations (taxes) were also considered as 1% of the total capital costs. These operational prices resulted in a total running treatment cost of USD 5.48/ m^3 .

3.10. Meeting the Sustainability Dimensions from the Photocatalytic Degradation of Dyes

The current study's outputs maintain several benefits that could fulfill the sustainability dimensions. For example, removing dye pollutants (e.g., MB) from the textile industrial effluents before final disposal tends to protect the aquatic environment. This aim has a positive correlation with SDG14 "Life Below Water" by protecting and conserving the aquatic species from marine pollution because dyes negatively affect the fish organs, such as the liver and gills, and reduce sunlight penetration and the related photosynthetic activities [6]. Moreover, this treatment facility could meet the targets of SDG3 "Good Health and Well-being" because textile dyes can enter the food chain through biomagnification and biotransformation [2]. Also, the study demonstrates that ANN is an innovative tool that could optimize the photocatalytic treatment facility and reduce the operational costs, meeting SDG9 "Industry, Innovation, and Infrastructure". Furthermore, using sunlight as an irradiation source (cleaner energy) and reusing the synthesized ZnO/MgO photocatalyst under six consecutive cycles complies with the targets of SDG12 "Responsible Consumption and Production". This SDG could also be improved by conducting essential research on the management and/or disposal of exhausted ZnO/MgO photocatalysts. For Instance, Razzaghian Ghadikolaee et al. [56] found that the photocatalyst material after exhaustion could be managed by using it as an attractive additive to maintain better 3D-printed concrete properties.

Despite the aforementioned benefits provided by photocatalytic dye degradation, some aspects related to the synthesis of the catalyst materials and their disposal after reuse should be addressed for enhancing the process's sustainability. Regarding the manufacturing methods, plant extracts [57] and microorganisms [58] have attracted much attention as reducing agents in the photocatalyst green synthesis process. Applying these eco-friendly and cleaner techniques to synthesize the ZnO/MgO could reduce the chemical costs and

minimize exposure to possible material toxicity. Where the recyclability of the spent catalyst material is concerned, the ZnO/MgO nanocomposite should be tested for applications as an additive in the construction industry, following previous research [56]. This benefit would avoid the unrestricted disposal of solid waste to the terrestrial and inland freshwater ecosystems and the related services, meeting the targets of SDG15 “Life on Land”. Assuming that the nanocomposite can neither be applied in construction nor in soil amendment, the spent ZnO and MgO can be treated by thorough washing to remove any adsorbed pollutants before disposal into well-designed and properly operated landfills.

4. Conclusions

This study succeeded in providing a promising artificial neural network (ANN) model that could cost-effectively optimize the photocatalytic dye degradation system. Operating the photocatalytic degradation process under the determined optimum conditions enhanced the methylene blue (MB) removal efficiency by $\approx 12\%$, while the treatment cost was reduced by about 7% compared with the unoptimized condition. The study outcomes also included the successful synthesis of a ZnO/MgO photocatalyst that had a narrower optical band gap and better surface morphology, functional groups, and crystal structure than ZnO and MgO individually. Hence, the proposed artificial intelligence technique can be beneficial for generating more accurate predictions of the photodegradation process in wastewater treatment while maintaining better operational conditions that provide higher economic benefits. Further studies are required to determine the degradation pathway and by-products generated, identify the ROS responsible for the photocatalytic degradation process, use green routes for ZnO/MgO synthesis, and enlarge the data set size for a more accurate ANN training process.

Supplementary Materials: The following supporting information can be downloaded at: <https://www.mdpi.com/article/10.3390/su16020529/s1>, Figure S1. Initial photocatalysis experiments under light irradiation; Figure S2. N_2 adsorption–desorption isotherms of (a) ZnO, (b) MgO, and (c) ZnO/MgO; Figure S3. Plot of actual versus predicted MB removal efficiencies; Figure S4. Optimization of photocatalysis independent variables using the response surface methodology (RSM) based on the quadratic regression model; Figure S5. Recyclability of the photocatalyst material; Figure S6. Effect of variation from -30% to 30% on the total treatment cost; Table S1. Chemicals and reagents used for experimental procedures. All chemicals were utilized in the experiments without further purification; Table S2. Selection of best number of neurons in the hidden layer (N) and transfer function based on the smallest MSE of different ANN models for predicting MB removal efficiencies. Here, *trainoss*: one step secant; *traincgb*: conjugate gradient with Powell–Beale restart; *trainbfg*: Broyden–Fletcher–Goldfarb–Shanno (BFGS) quasi-Newton; *trainlm*: Levenberg–Marquardt; *trainscg*: scaled conjugate gradient; *traincgf*: Fletcher–Powell conjugate gradient; *traingd*: gradient descent back-propagation; Table S3. Optimum weights and biases of the feed-forward back-propagation ANN (4–8–1) with *trainlm* training function used to predict the MB R(%). Reference [59] is cited in the supplementary materials.

Author Contributions: Conceptualization, A.A., M.F. and M.N.; methodology, K.F.N.; formal analysis, K.F.N.; writing—original draft preparation, K.F.N.; writing—review and editing, A.A., M.F. and M.N.; visualization, A.A., M.F. and M.N.; supervision, A.A., M.F. and M.N. All authors have read and agreed to the published version of the manuscript.

Funding: This research was funded by funds that were partially supported by TICAD7, Egypt-Japan University of Science and Technology (E-JUST), and Japan International Cooperation Agency (JICA).

Institutional Review Board Statement: Not applicable.

Informed Consent Statement: Not applicable.

Data Availability Statement: The data that support the findings of this study are available within the article (and/or) its Supplementary Materials.

Acknowledgments: The first author is very grateful to TICAD7 for providing financial support in the form of an MSc. scholarship. Also, thanks to JICA-Japan International Cooperation Agency for providing all facilities and equipment to accomplish this study.

Conflicts of Interest: The authors declare no conflicts of interest.

References

- Wang, B.; Suen, H.; Zhang, B. Hydrodynamic cavitation as a promising route for wastewater treatment—A Review. *Chem. Eng. J.* **2022**, *412*, 128685. [\[CrossRef\]](#)
- Vasiljevic, Z.Z.; Dojcinovic, M.P.; Vujanecic, J.D.; Jankovic-Castvan, I.; Ognjanovic, M.; Tadic, N.B.; Stojadinovic, S.; Nikolic, M.V.; Brankovic, G.O. Photocatalytic degradation of methylene blue under natural sunlight using iron titanate nanoparticles prepared by a modified sol-gel method: Methylene blue degradation with Fe₂TiO₅. *R. Soc. Open Sci.* **2020**, *7*, 200708. [\[CrossRef\]](#) [\[PubMed\]](#)
- Yang, L.; Zhao, Z.; Wang, H.; Cai, Z. Synthesis of ZnO/ZnS core/shell microsphere and its photocatalytic activity for methylene blue and eosin dyes degradation. *J. Dispers. Sci. Technol.* **2020**, *41*, 2152–2158. [\[CrossRef\]](#)
- Moorthy, K.; Rath, B.G.; Shukla, S.P.; Kumar, K.; Bharti, V.S. Acute toxicity of textile dye Methylene blue on growth and metabolism of selected freshwater microalgae. *Environ. Toxicol. Pharmacol.* **2021**, *82*, 103552. [\[CrossRef\]](#) [\[PubMed\]](#)
- Khan, I.; Saeed, K.; Zekker, I.; Zhang, B.; Hendi, A.H.; Ahmad, A.; Ahmad, S.; Zada, N.; Ahmad, H.; Shah, L.A.; et al. Review on Methylene Blue: Its Properties, Uses, Toxicity and Photodegradation. *Water* **2022**, *14*, 242. [\[CrossRef\]](#)
- Alkaykh, S.; Mbarek, A.; Ali-Shattle, E.E. Photocatalytic degradation of methylene blue dye in aqueous solution by MnTiO₃ nanoparticles under sunlight irradiation. *Heliyon* **2020**, *6*, e03663. [\[CrossRef\]](#) [\[PubMed\]](#)
- Karim, M.A.; Aziz, K.H.; Omer, K.M.; Salih, Y.M.; Mustafa, F.; Rahman, K.O.; Mohammad, Y. Degradation of aqueous organic dye pollutants by heterogeneous photo-assisted Fenton-like process using natural mineral activator: Parameter optimization and degradation kinetics. In Proceedings of the 7th International Conference on Water Resource and Environment (WRE 2021), Xi'an, China, 1–4 November 2021; Volume 958.
- Mendis, A.; Thambiliyagodage, C.; Ekanayake, G.; Liyanaarachchi, H.; Jayanetti, M.; Vigneswaran, S. Fabrication of Naturally Derived Chitosan and Ilmenite Sand-Based TiO₂/Fe₂O₃/Fe-N-Doped Graphitic Carbon Composite for Photocatalytic Degradation of Methylene Blue under Sunlight. *Molecules* **2023**, *28*, 3154. [\[CrossRef\]](#)
- Karimi, M.A.; Hatefi-Mehrjardi, A.; Askarpour Kabir, A.; Zaydabadi, M. Synthesis, characterization, and application of MgO/ZnO nanocomposite supported on activated carbon for photocatalytic degradation of methylene blue. *Res. Chem. Intermed.* **2014**, *41*, 6157–6168. [\[CrossRef\]](#)
- Hama Aziz, K.H.; Omer, K.M.; Mahyar, A.; Miessner, H.; Mueller, S.; Moeller, D. Application of Photocatalytic Falling Film Reactor to Elucidate the Degradation Pathways of Pharmaceutical Diclofenac and Ibuprofen in Aqueous Solutions. *Coatings* **2019**, *9*, 465. [\[CrossRef\]](#)
- Wen, L.; Wang, D.; Xi, J.; Tian, F.; Liu, P.; Bai, Z.W. Heterometal modified Fe₃O₄ hollow nanospheres as efficient catalysts for organic transformations. *J. Catal.* **2022**, *413*, 779–785. [\[CrossRef\]](#)
- Akpan, U.G.; Hameed, B.H. Parameters affecting the photocatalytic degradation of dyes using TiO₂-based photocatalysts: A review. *J. Hazard. Mater.* **2009**, *170*, 520–529. [\[CrossRef\]](#) [\[PubMed\]](#)
- Ren, G.; Han, H.; Wang, Y.; Liu, S.; Zhao, J.; Meng, X.; Li, Z. Recent Advances of Photocatalytic Application in Water Treatment: A Review. *Nanomaterials* **2021**, *11*, 1804. [\[CrossRef\]](#) [\[PubMed\]](#)
- Liyanaarachchi, H.; Thambiliyagodage, C.; Liyanaarachchi, C.; Samarakoon, U. Efficient photocatalysis of Cu doped TiO₂/g-C₃N₄ for the photodegradation of methylene blue. *Arab. J. Chem.* **2023**, *16*, 104749. [\[CrossRef\]](#)
- Gracien, E.B.; Jérémie, M.L.; Joseph, L.K.-K.; Omer, M.M.; Antoine, M.K.; Hercule, K.M.; Gerard, M.N. Role of hydroxyl radical scavenger agents in preparing silver nanoparticles under γ -irradiation. *SN Appl. Sci.* **2019**, *1*, 961. [\[CrossRef\]](#)
- Wu, H.; Gao, C.; Ma, L.; Wang, L. Controllable microemulsion method for the synthesis of Mg(OH)₂/PS core-shell structures. *Micro Nano Lett.* **2021**, *16*, 413–418. [\[CrossRef\]](#)
- Mohamed, O.A.; Masood, S.H.; Bhowmik, J.L. Optimization of fused deposition modeling process parameters for dimensional accuracy using I-optimality criterion. *Meas. J. Int. Meas. Confed.* **2016**, *81*, 174–196. [\[CrossRef\]](#)
- Amani-Ghadim, A.R.; Aber, S.; Olad, A.; Ashassi-Sorkhabi, H. Optimization of electrocoagulation process for removal of an azo dye using response surface methodology and investigation on the occurrence of destructive side reactions. *Chem. Eng. Process. Process Intensif.* **2013**, *64*, 68–78. [\[CrossRef\]](#)
- Bakr, M.; Nasr, M.; Ashmawy, M.; Tawfik, A. Predictive performance of auto-aerated immobilized biomass reactor treating anaerobic effluent of cardboard wastewater enriched with bronopol (2-bromo-2-nitropropan-1,3-diol) via artificial neural network. *Environ. Technol. Innov.* **2021**, *21*, 101327. [\[CrossRef\]](#)
- Alalm, M.G.; Nasr, M. Artificial intelligence, regression model, and cost estimation for removal of chlorothalonil pesticide by activated carbon prepared from casuarina charcoal. *Sustain. Environ. Res.* **2018**, *28*, 101–110. [\[CrossRef\]](#)
- Sadeghi, M.; Heydari, M.; Javanbakht, V. Photocatalytic and photo-fenton processes by magnetic nanophotocatalysts for efficient dye removal. *J. Mater. Sci. Mater. Electron.* **2021**, *32*, 5065–5081. [\[CrossRef\]](#)
- Meenakshi, S.; Rajarajan, M.; Rajendran, S.; Kennedy, Z.R.; Brindha, G. Synthesis and characterization of magnesium oxide nanoparticles. *Chem. Mater. Sci.* **2012**, *50*, 10618–10620.

23. Subalakshmi, A.; Kavitha, B.; Srinivasan, N.; Rajarajan, M.; Suganthi, A. An affordable efficient SrWO₄ decorated Bi₂O₃ nanocomposite: Photocatalytic activity for the degradation of methylene blue under visible light irradiation. *Mater. Today Proc.* **2022**, *48*, 409–419. [\[CrossRef\]](#)
24. Vishwanathan, S.; Das, S. Glucose-mediated one-pot hydrothermal synthesis of hollow magnesium oxide-zinc oxide (MgO-ZnO) microspheres with enhanced natural sunlight photocatalytic activity. *Environ. Sci. Pollut. Res.* **2023**, *30*, 8512–8525. [\[CrossRef\]](#) [\[PubMed\]](#)
25. Saoud, K.M.; Saeed, S.; Al-Soubaihi, R.; Bertino, M. Microwave Assisted Preparation of Magnesium Hydroxide Nano-sheets. *Am. J. Nanomater.* **2014**, *2*, 21–25.
26. Mustapha, S.; Ndamitso, M.; Abdulkareem, A.; Tijani, J.; Shuaib, D.; Mohammed, A.; Sumaila, A. Comparative study of crystallite size using Williamson-Hall and Debye-Scherrer plots for ZnO nanoparticles. *Adv. Nat. Sci. Nanosci. Nanotechnol.* **2019**, *10*, 045013. [\[CrossRef\]](#)
27. Yousefi, S.; Ghasemi, B. Precipitator concentration-dependent opto-structural properties of MgO nanoparticles fabricated using natural brine. *SN Appl. Sci.* **2020**, *2*, 852. [\[CrossRef\]](#)
28. Sangeeta, M.; Karthik, K.V.; Ravishankar, R.; Anantharaju, K.S.; Nagabhushana, H.; Jeetendra, K.; Vidya, Y.S.; Renuka, L. Synthesis of ZnO, MgO and ZnO/MgO by Solution Combustion Method: Characterization and Photocatalytic Studies. *Mater. Today Proc.* **2017**, *4*, 11791–11798. [\[CrossRef\]](#)
29. Ansari, A.; Ali, A.; Asif, M.; Shamsuzzaman, A. Microwave-assisted MgO NP catalyzed one-pot multicomponent synthesis of polysubstituted steroidal pyridines. *New J. Chem.* **2018**, *42*, 184–197. [\[CrossRef\]](#)
30. Mensah, K.; Samy, M.; Ezz, H.; Elkady, M.; Shokry, H. Utilization of iron waste from steel industries in persulfate activation for effective degradation of dye solutions. *J. Environ. Manag.* **2022**, *314*, 7. [\[CrossRef\]](#)
31. Munawar, T.; Mukhtar, F.; Yasmeen, S.; Naveed-ur-Rehman, M.; Nadeem, M.S.; Riaz, M.; Mansoor, M.; Iqbal, F. Sunlight-induced photocatalytic degradation of various dyes and bacterial inactivation using CuO–MgO–ZnO nanocomposite. *Environ. Sci. Pollut. Res.* **2021**, *28*, 42243–42260. [\[CrossRef\]](#)
32. Arora, A.K.; Devi, S.; Jaswal, V.S.; Singh, J.; Kinger, M.; Gupta, V.D. Synthesis and characterization of ZnO nanoparticles. *Orient. J. Chem.* **2014**, *30*, 1671–1679. [\[CrossRef\]](#)
33. Ajeesha, T.; Ashwini, A.; George, M.; Manikandan, A.; Mary, J.; Slimani, Y.; Almessiere, M.; Baykal, A. Nickel substituted MgFe₂O₄ nanoparticles via co-precipitation method for photocatalytic applications. *Phys. B Condens. Matter* **2021**, *606*, 412660. [\[CrossRef\]](#)
34. Yang, X.-H.; Sun, S.-Y.; Fu, H.-T.; Li, W.-F.; An, X.-Z. Two-Step Fabrication of Porous α -Fe₂O₃@ δ -TiO₂ core-shell Nanostructures with Enhanced Photocatalytic Activity. In Proceedings of the 3rd Annual International Conference on Advanced Material Engineering (AME 2017), Shanghai, China, 14–16 April 2017.
35. Makuła, P.; Pacia, M.; Macyk, W. How To Correctly Determine the Band Gap Energy of Modified Semiconductor Photocatalysts Based on UV–Vis Spectra. *J. Phys. Chem. Lett.* **2018**, *9*, 6814–6817. [\[CrossRef\]](#) [\[PubMed\]](#)
36. Azadi, S.; Karimi-Jashni, A.; Javadpour, S. Modeling and optimization of photocatalytic treatment of landfill leachate using tungsten-doped TiO₂ nano-photocatalysts: Application of artificial neural network and genetic algorithm. *Process Saf. Environ. Prot.* **2018**, *117*, 267–277. [\[CrossRef\]](#)
37. Garson, G. Interpreting neural-network connection weights. *AI Expert* **1991**, *6*, 46–51.
38. Kalaycıoğlu, Z.; Uysal, Ö.; Pekcan, Ö.; Erim, F.B. Efficient Photocatalytic Degradation of Methylene Blue Dye from Aqueous Solution with Cerium Oxide Nanoparticles and Graphene Oxide-Doped Polyacrylamide. *ASC Omega J.* **2023**, *8*, 13004–13015. [\[CrossRef\]](#) [\[PubMed\]](#)
39. Sousa, H.R.; Silva, L.S.; Sousa, P.A.A.; Sousa, R.R.M.; Fonseca, M.G.; Osajima, J.A.; Silva-Filho, E.C. Evaluation of methylene blue removal by plasma activated palygorskites. *J. Mater. Res. Technol.* **2019**, *8*, 5432–5442. [\[CrossRef\]](#)
40. Kumar, A.; Pandey, G. The photocatalytic degradation of Methyl Green in presence of Visible light with photoactive Ni_{0.10}:La_{0.05}:TiO₂ nanocomposites. *IOSR J. Appl. Chem.* **2017**, *10*, 31–44.
41. Xue, H.; Jiang, Y.; Yuan, K.; Yang, T.; Hou, J.; Cao, C.; Feng, K.; Wang, X. Floating photocatalyst of B-N-TiO₂/expanded perlite: A sol-gel synthesis with optimized mesoporous and high photocatalytic activity. *Sci. Rep.* **2016**, *6*, 29902. [\[CrossRef\]](#)
42. Lagergren, S. Zur Theorie der sogenannten Adsorption gelöster Stoffe. *K. Sven. Vetenskapsakad. Handl.* **1898**, *24*, 1–39.
43. Habibi, M.; Habibi-Yangjeh, A.; Pouran, S.R.; Chand, H.; Krishnan, V.; Xu, X.; Wang, C. Visible-light-triggered persulfate activation by CuCo₂S₄ modified ZnO photocatalyst for degradation of tetracycline hydrochloride. *Colloids Surf. A Physicochem. Eng. Asp.* **2022**, *642*, 128640. [\[CrossRef\]](#)
44. Zhu, F.; Ma, J.; Ji, Q.; Cheng, H.; Komarneni, S. Visible-light-driven activation of sodium persulfate for accelerating orange II degradation using ZnMn₂O₄ photocatalyst. *Chemosphere* **2021**, *278*, 130404. [\[CrossRef\]](#) [\[PubMed\]](#)
45. Zhou, X.; Zhu, Y.; Niu, Q.; Zeng, G.; Lai, C.; Liu, S.; Huang, D.; Qin, L.; Liu, X.; Li, B.; et al. New notion of biochar: A review on the mechanism of biochar applications in advanced oxidation processes. *Chem. Eng. J.* **2021**, *416*, 129027. [\[CrossRef\]](#)
46. Revathi, V.; Karthik, K. Microwave assisted CdO–ZnO–MgO nanocomposite and its photocatalytic and antibacterial studies. *J. Mater. Sci. Mater. Electron.* **2018**, *29*, 18519–18530. [\[CrossRef\]](#)
47. Panchal, P.; Paul, D.R.; Malik, R.; Sharma, A.; Meena, P.; Patidar, D.; Nehra, S. Phytoextract Mediated ZnO/MgO Nanocomposites for Photocatalytic and Antibacterial Activities. *J. Photochem. Photobiol. A Chem.* **2019**, *385*, 112049. [\[CrossRef\]](#)

48. Xiang, X.; Xie, L.; Li, Z.; Li, F. Ternary MgO/ZnO/In₂O₃ heterostructured photocatalysts derived from a layered precursor and visible-light-induced photocatalytic activity. *Chem. Eng. J.* **2013**, *221*, 222–229. [[CrossRef](#)]
49. Ansari, F.; Nasr, M.; Rawat, I.; Bux, F. Artificial neural network and techno-economic estimation with algae-based tertiary wastewater treatment. *J. Water Process Eng.* **2021**, *40*, 101761. [[CrossRef](#)]
50. León, M.; Silva, J.; Carrasco, S.; Barrientos, N. Design, Cost Estimation and Sensitivity Analysis for a Production Process of Activated Carbon from Waste Nutshells by Physical Activation. *Processes* **2020**, *8*, 945. [[CrossRef](#)]
51. Ansari, F.A.; Ravindran, B.; Gupta, S.K.; Nasr, M.; Rawat, I.; Bux, F. Techno-economic estimation of wastewater phycoremediation and environmental benefits using *Scenedesmus obliquus* microalgae. *J. Environ. Manag.* **2019**, *240*, 293–302. [[CrossRef](#)]
52. Mahamuni, N.N.; Adewuyi, Y.G. Advanced oxidation processes (AOPs) involving ultrasound for waste water treatment: A review with emphasis on cost estimation. *Ultrason. Sonochem.* **2010**, *17*, 990–1003. [[CrossRef](#)]
53. Hamdy, A.; Mostafa, M.K.; Nasr, M. Zero-valent iron nanoparticles for methylene blue removal from aqueous solutions and textile wastewater treatment, with cost estimation. *Water Sci. Technol.* **2018**, *78*, 367–378. [[CrossRef](#)] [[PubMed](#)]
54. Vishnuganth, M.; Remya, N.; Kumar, M.; Selvaraju, N. Photocatalytic degradation of carbofuran by TiO₂-coated activated carbon: Model for kinetic, electrical energy per order and economic analysis. *J. Environ. Manag.* **2016**, *181*, 201–207. [[CrossRef](#)] [[PubMed](#)]
55. Olya, M.E.; Akhi, Y.; Marandi, R. Improvement of efficiency and electrical energy consumption of AB74 degradation process using a novel cylindrical batch photochemical reactor. *Orient. J. Chem.* **2016**, *32*, 1295–1303. [[CrossRef](#)]
56. Ghadikolaei, M.R.; Cerro-Prada, E.; Pan, Z.; Korayem, A.H. Nanomaterials as Promising Additives for High-Performance 3D-Printed Concrete: A Critical Review. *Nanomaterials* **2023**, *13*, 1440. [[CrossRef](#)]
57. Tesfaye, M.; Gonfa, Y.; Tadesse, G.; Temesgen, T.; Periyasamy, S. Green synthesis of silver nanoparticles using *Vernonia amygdalina* plant extract and its antimicrobial activities. *Heliyon* **2023**, *9*, e17356. [[CrossRef](#)]
58. Lobregas, M.; Camacho, D. Green synthesis of copper-based nanoparticles using microbes. *Copp. Nanostructures Next-Gener. Agrochem. Sustain. Agroecosyst.* **2022**, *2022*, 17–44. [[CrossRef](#)]
59. Ajmal, A.; Majeed, I.; Malik, R.N.; Idriss, H.; Nadeem, M.A. Principles and mechanisms of photocatalytic dye degradation on TiO₂ based photocatalysts: A comparative overview. *RSC Adv.* **2014**, *4*, 37003–37026. [[CrossRef](#)]

Disclaimer/Publisher's Note: The statements, opinions and data contained in all publications are solely those of the individual author(s) and contributor(s) and not of MDPI and/or the editor(s). MDPI and/or the editor(s) disclaim responsibility for any injury to people or property resulting from any ideas, methods, instructions or products referred to in the content.